Article

Coherent coupling and non-destructive measurement of trapped-ion mechanical oscillators

Check for updates

Pan-Yu Hou [1,2,4] ✉, Jenny J. Wu [1,2], Stephen D. Erickson[1,2,5], Daniel C. Cole[1,6], Giorgio Zarantonello [1,2,7,8], Adam D. Brandt [1], Shawn Geller [1,2], Alex Kwiatkowski [1,2], Scott Glancy [1], Emanuel Knill[1,3], Andrew C. Wilson [1], Daniel H. Slichter [1] & Dietrich Leibfried[1] ✉

Precise quantum control and measurement of several harmonic oscillators, such as the modes of the electromagnetic field in a cavity or of mechanical motion, are key for their use as quantum platforms. The motional modes of trapped ions can be individually controlled and have good coherence properties. However, achieving high-fidelity two-mode operations and non-destructive measurements of the motional state has been challenging. Here we demonstrate the coherent exchange of single motional quanta between spectrally separated harmonic motional modes of a trapped-ion crystal. The timing, strength, and phase of the coupling are controlled through an oscillating electric potential with suitable spatial variation. Coupling rates that are much larger than decoherence rates enable demonstrations of high-fidelity quantum state transfer and beam-splitter operations, entanglement of motional modes, and Hong–Ou–Mandel-type interference. Additionally, we use the motional coupling to enable repeated non-destructive projective measurement of a trapped-ion motional state. Our work enhances the suitability of trapped-ion motion for continuous-variable quantum computing and error correction and may provide opportunities to improve the performance of motional cooling and motion-mediated entangling interactions.

Harmonic oscillators (HOs) are ubiquitous in models of nature, and many elementary phenomena can be described by the interaction between HOs. The high-dimensional Hilbert space of HOs can be used to encode and process quantum information, given control operations of sufficient fidelity[1–13]. Quantum error-correcting codes can take advantage of this large Hilbert space to reduce hardware requirements relative to codes based on two-level systems[9,11,14–16]. Individual control and coherent coupling of HOs near or in the quantum regime have been demonstrated across many physical systems[17–35]. Among them, modes of trapped-ion motion[36,37] and of superconducting cavities in the circuit quantum electrodynamics architecture[30,38,39] exhibit long coherence times and can be individually controlled with high fidelity, as required for continuous-variable quantum information processing. Bosonic quantum error correction beyond the break-even point has recently been demonstrated in circuit quantum electrodynamics systems[40,41].

[1]National Institute of Standards and Technology, Boulder, CO, USA. [2]Department of Physics, University of Colorado, Boulder, CO, USA. [3]Center for Theory of Quantum Matter, University of Colorado, Boulder, CO, USA. [4]Present address: Center for Quantum Information, Institute for Interdisciplinary Information Sciences, Tsinghua University, Beijing, People's Republic of China. [5]Present address: Quantinuum, Broomfield, CO, USA. [6]Present address: ColdQuanta Inc, Boulder, CO, USA. [7]Present address: QUDORA Technologies GmbH, Braunschweig, Germany. [8]Present address: Institute of Quantum Optics, Leibniz University Hannover, Hannover, Germany. ✉e-mail: houpanyu0226@gmail.com; dietrich.leibfried@nist.gov
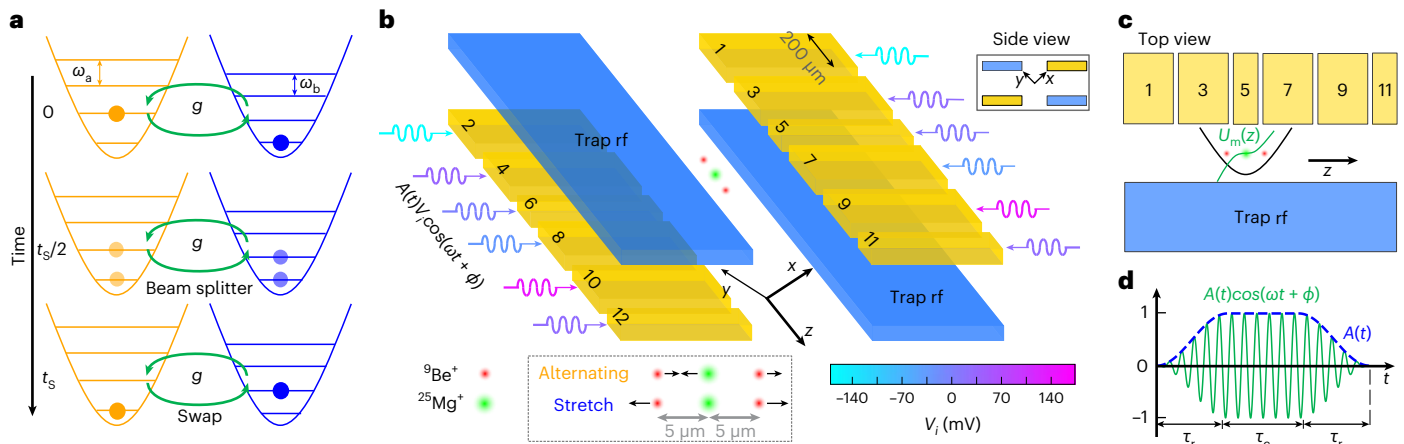
Fig. 1 | Coupled quantum mechanical oscillators. a, Illustration of quantum state transfer between two coupled HOs. Coherent coupling (green) fully exchanges states up to a phase at t_s and creates two-mode entanglement at $t_s/2$, which constitutes a beam-splitter operation (equation (1) and Methods). **b,c**, Three-dimensional perspective, side view (inset; **b**) and top view (**c**) of trapping zone in a segmented Paul trap (not to scale) with radio-frequency voltages applied to two electrodes (blue, 'trap rf'). A ^{9}Be$^+$–^{25}Mg$^+$–^{9}Be$^+$ crystal is confined along axial direction z in a harmonic potential (solid black line in top view). Two of three axial normal modes, an alternating mode at 3.66 MHz and a stretch mode at 3.38 MHz (mode participation vectors ξ for all ions visualized as arrows in the dashed box at the bottom), are coupled by an oscillating electric

potential $U_{mod}(z,t) = U_m(z)A(t)\cos(\omega t + \phi)$. The coordinate origin is at the Mg$^+$ ion, and the spatial dependence of $U_m(z) \propto z^3$ is visualized by the green curve in **c**. The potential is generated from synchronized oscillating drives $V_i A(t)\cos(\omega t + \phi)$ for $i \in \{1, ..., 12\}$ applied to 12 control electrodes (gold). The V_i values are represented by the colour of the wavy arrows and correspond to a coupling rate of $2g_0 = 2\pi \times 5.1$ kHz when $A(t) = 1$. **d**, Coupling pulse shape in experiments. The green oscillating line represents the temporal dependence of $U_{mod}(z,t)$ with amplitude envelope $A(t)$ (blue dashed line). For a coupling pulse with non-zero duration, $A(t)$ ramps up from zero to one in $\tau_r = 20$ μs, stays constant for τ_c and ramps back to zero in τ_r. The pulse area is equal to that of a square pulse of amplitude one and duration $\tau = \tau_r + \tau_c$.

Continuous-variable quantum information processing in trapped-ion systems is at present limited by the lack of controllable direct coupling between motional modes for two-mode operations and of methods for making non-destructive measurements of motional states. The latter is a prerequisite for quantum error correction based on error syndrome measurement and has been a long-standing short-coming[36,42,43] because photon recoil during atomic state fluorescence read-out stochastically alters the motion of the addressed ion and scrambles any information stored in its motional state. Previous work has relied on probabilistic state preparation and measurement through the post-selection of 'dark' read-out events (without photon scattering)[42,44,45] or on dissipative state preparation that does not involve detection[43].

The motional modes of ions have been coupled through the ions' internal (electronic) states using lasers, but this does not work for ions that do not have laser-accessible transitions or do not participate in the modes to be coupled[45–47]. The motional modes of ions in separate potential wells have also been resonantly coupled by the Coulomb interaction, with the coupling strength limited by the ion–ion spacing and restricted control[17–20], and modulation of the trap potential has been used to couple two motional modes of an electron cloud or a single trapped ion[21,48].

Here, we demonstrate direct coupling—with controllable timing, strength, and phase—between two motional modes in a linear mixed-species ion crystal. The duration of state exchange can be much shorter than motional coherence times, enabling high-fidelity two-mode operations. The coupling is generated by a suitable spatially varying oscillating electric potential, can be used for crystals of arbitrary size, and is independent of ion internal structure, making it applicable to any Coulomb crystal, including those containing molecular ions, highly charged ions, or other species that lack easily accessible transitions between internal states. More generally, well-controlled mode coupling can be used to improve cooling and quantum logic operations for ion-based quantum information processing, timekeeping and quantum sensing applications[49].

We also use mode coupling to perform repeated non-destructive measurements of ion motion. For ion crystals with a mirror symmetry

around the centre ion, this ion must have zero amplitude in all modes with an even motion pattern. Even modes are, therefore, 'protected' from the recoil of the centre ion. By the same argument, the modes that do not suffer recoils from the centre ion are inaccessible through that ion. Mode coupling enables us to transfer information about a motional state onto the centre ion, swap the state of motion into a protected mode and then read out the centre ion (thus learning information about the motional state of interest) without destroying the motional state due to photon recoils. This protocol can then be repeated to achieve greater confidence in the result or to realize repeated rounds of syndrome measurement for a bosonic error-correcting code.

Results

A linear string of N ions confined in a three-dimensional harmonic potential exhibits $3N$ normal modes of collective motion that can be treated as uncoupled HOs[36,50]. Consider two normal modes a and b at frequencies ω_a and ω_b, with ladder operators $\hat{a}$ and $\hat{b}$. Their coupling can be described by a Hamiltonian:

$$H = \hbar g \left(e^{i\phi} \hat{a}\hat{b}^\dagger + e^{-i\phi} \hat{b}\hat{a}^\dagger \right), \tag{1}$$

where $2\pi\hbar$ is Planck's constant, $\hbar g$ is the coupling energy, and ϕ is the coupling phase. This coupling leads to state exchange between modes a and b, as illustrated in Fig. 1a. Ideally, the timing, strength g, and phase ϕ of the coupling can be controlled well.

To couple modes, we add to the existing confining trap potential an oscillating and spatially varying electric potential modulation of the form

$$U_{mod}(\mathbf{r}, t) = U_m(\mathbf{r})A(t)\cos(\omega t + \phi), \tag{2}$$

with $\omega \approx |\omega_a - \omega_b|$ and $0 \le A(t) \le 1$. The smooth envelope $A(t)$ (blue dashed line in Fig. 1d) evolves slowly compared to $2\pi/\omega$ to avoid sudden perturbations of the trapping potential. Modes are coupled by curvature terms
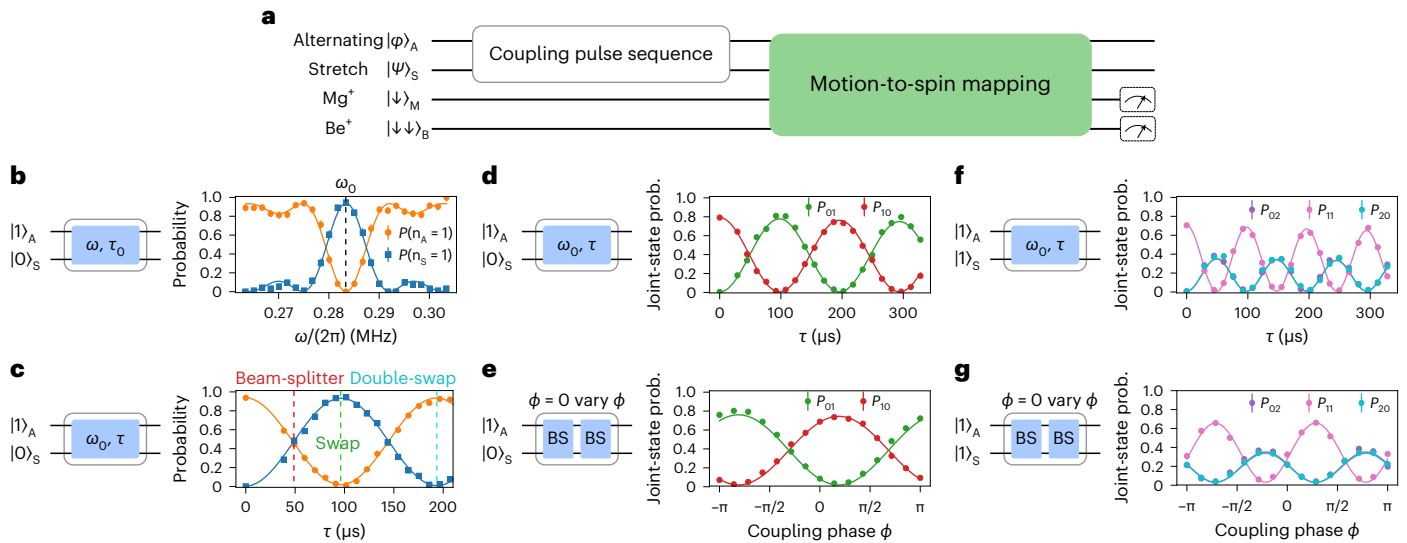
Fig. 2 | Coherent coupling dynamics. a, Experimental sequence for characterizing alternating–stretch coupling. Modes are prepared by Raman laser interactions, then coupled by the pulse sequence in the white box. Motional state probabilities are mapped onto internal states of one or both ion species by further Raman laser interactions (green box, see details in text) followed by state-dependent fluorescence detection. Initial motional states and pulse sequences (one blue box per coupling pulse) are indicated in **b**–**g**. Lines in **b** and **c** are fits to data, while lines in **d**–**g** are from numerical simulations using experimental parameters. **b**, With initial state $|1\rangle_A|0\rangle_S$, $P(n_A = 1)$ is high unless the coupling frequency ω is tuned near resonance; otherwise the probability of the phonon being found in the stretch mode is high (blue squares). **c**, With the coupling on resonance, a single phonon is coherently swapped between the two modes as the coupling time τ increases. Vertical dashed lines indicate pulse durations for beam-splitter (BS), swap and double-swap operations. **d**–**g**, Probability of finding certain states as the exchange duration τ is varied for initial states $|1\rangle_A|0\rangle_S$ (**d**) and $|1\rangle_A|1\rangle_S$ (**f**), or as the coupling phase is varied for initial states $|1\rangle_A|0\rangle_S$ (**e**) and $|1\rangle_A|1\rangle_S$ (**g**). Labels P_{as} indicate that there are a phonons in the alternating mode and s phonons in the stretch mode. Results in **d**,**e** and **f**,**g** verify two-mode entanglement generated by a beam splitter. Results in **f** and **g** correspond to Hong–Ou–Mandel-type interference between two phonons at different frequencies. Each data point was obtained from 300 experiments in **b**,**c** and from 1,000 experiments in **d**–**g**, with a 68% confidence error bar. prob., probability.

$$\alpha_n = \frac{\partial^2 U_m}{\partial i_a \partial i_b}\Big|_{\mathbf{r}=\mathbf{r}_{n,0}} \tag{3}$$

in the expansion of $U_m(\mathbf{r})$ around the nth ion's equilibrium position $\mathbf{r}_{n,0}$ along the mode directions $i_a, i_b \in \{x, y, z\}$. The coupling strength g_0 is a sum over contributions from each ion:

$$g_0 = \sum_{n=1}^{N} g_n = \sum_{n=1}^{N} \left(\frac{Q_n}{4M_n\sqrt{\omega_a \omega_b}} \times \alpha_n \xi_{n,a}^{(i_a)} \xi_{n,b}^{(i_b)} \right), \tag{4}$$

where Q_n, M_n, $\xi_{n,a}^{(i_a)}$ and $\xi_{n,b}^{(i_b)}$ denote the charge, mass, and participations in modes a and b of the nth ion. The participation is defined as the nth ion's component of the normalized eigenvector of a given normal mode. After transforming into the interaction picture and neglecting fast-rotating terms (Methods), the Hamiltonian associated with the modulation in equation (2) becomes equation (1) with $g(t) = A(t)g_0$. A suitable choice of $U_m(\mathbf{r})$ sets the signs of the products $\alpha_n \xi_{n,a}^{(i_a)} \xi_{n,b}^{(i_b)}$ so that the g_n add constructively.

We trap $^9\text{Be}^+$ and $^{25}\text{Mg}^+$ ions in the segmented linear Paul trap shown in Fig. 1b,c (see also ref. 51). We denote the linear trap axis as z and the trap potential ellipsoid radial principal axes as x and y. To produce the coupling potential $U_{\text{mod}}(\mathbf{r}, t)$, we apply voltages of the form $V_i A(t)\cos(\omega t + \phi)$, $i \in \{1, ..., 12\}$, to the 12 electrodes closest to the ions, using simulations of the potentials created by each electrode at the ion positions to determine the desired V_i. In each experiment, $^9\text{Be}^+$ is prepared in $|\downarrow\rangle_B \equiv {}^2S_{1/2}|F = 2, m_F = 2\rangle_B$ and $^{25}\text{Mg}^+$ in $|\downarrow\rangle_M \equiv {}^2S_{1/2}|F = 3, m_F = 3\rangle_M$ by optical pumping. Transitions to the other qubit states $|\uparrow\rangle_B \equiv {}^2S_{1/2}|F = 1, m_F = 1\rangle_B$ and $|\uparrow\rangle_M \equiv {}^2S_{1/2}|F = 2, m_F = 2\rangle_M$ are driven by microwave magnetic fields or Raman laser beams. Motional mode information is mapped into internal states using sideband transitions[36] and read out by state-dependent fluorescence. Ions in the 'bright' states $|\downarrow\rangle_B$ and $|\downarrow\rangle_M$ scatter thousands of photons during the read-out, of which

approximately 30 photons on average are detected, whereas all other hyperfine states ('dark' states) scatter zero or a few photons. Further details are provided in Supplementary Section 1.

We demonstrate the essential features of the coupling on the alternating (~3.66 MHz, subscript A) and stretch (~3.38 MHz, subscript S) axial modes of a $^9\text{Be}^+$–$^{25}\text{Mg}^+$–$^9\text{Be}^+$ mixed-species crystal. The participations of ions in each mode are represented by black arrows in the lowest panel of Fig. 1b. The Mg$^+$ ion does not contribute to g_0 because it does not participate in the stretch mode. A cubic oscillating potential $U_{\text{mod}}(z, t) = A(t)U_m(z)\cos(\omega t + \phi) \propto z^3$ yields opposite α_n for the two Be$^+$ ions, so that the g_n add constructively.

The sequence of operations for characterizing the coupling is shown in Fig. 2a. We calibrate the optimal modulation frequency ω_0 and the coupling strength g_0 by preparing the two modes in the state $|1\rangle_A|0\rangle_S$. A coupling pulse alters the probability $P(n_{A/S} = 1)$ of which mode contains the motional quantum (phonon). When scanning the modulation frequency ω (Fig. 2b) around $\omega_A - \omega_S$ with fixed coupling pulse duration $\tau_0 \approx 100~\mu\text{s}$, the probability $P(n_A = 1)$ is reduced to near zero coincident with an increase of the probability $P(n_S = 1)$. With the drive frequency fixed at ω_0, we scan the pulse duration τ, observing $P(n_A = 1)$ and $P(n_S = 1)$ oscillating out of phase at frequency $\Omega_c = 2g_0 \approx 2\pi \times 5.1~\text{kHz}$, as shown in Fig. 2c. The single phonon is swapped into the stretch mode at $t_s \approx 100~\mu\text{s}$ and transferred back to the alternating mode ('double-swap') at $2t_s$. The loss of population from the $n = \{0, 1\}$ subspace per swap is estimated to be about 0.5%, mainly due to motional heating into states with $n > 1$ (Supplementary Section 2). We can attain a maximum coupling frequency Ω_c of about $2\pi \times 18~\text{kHz}$, which is limited by the drive electronics (Methods).

The dynamics of coherent coupling are characterized by measuring correlations between coupled motional modes. For each of the two modes, we map the amplitudes of specific number states onto the internal states of one ion species, with the other mode mapped to the
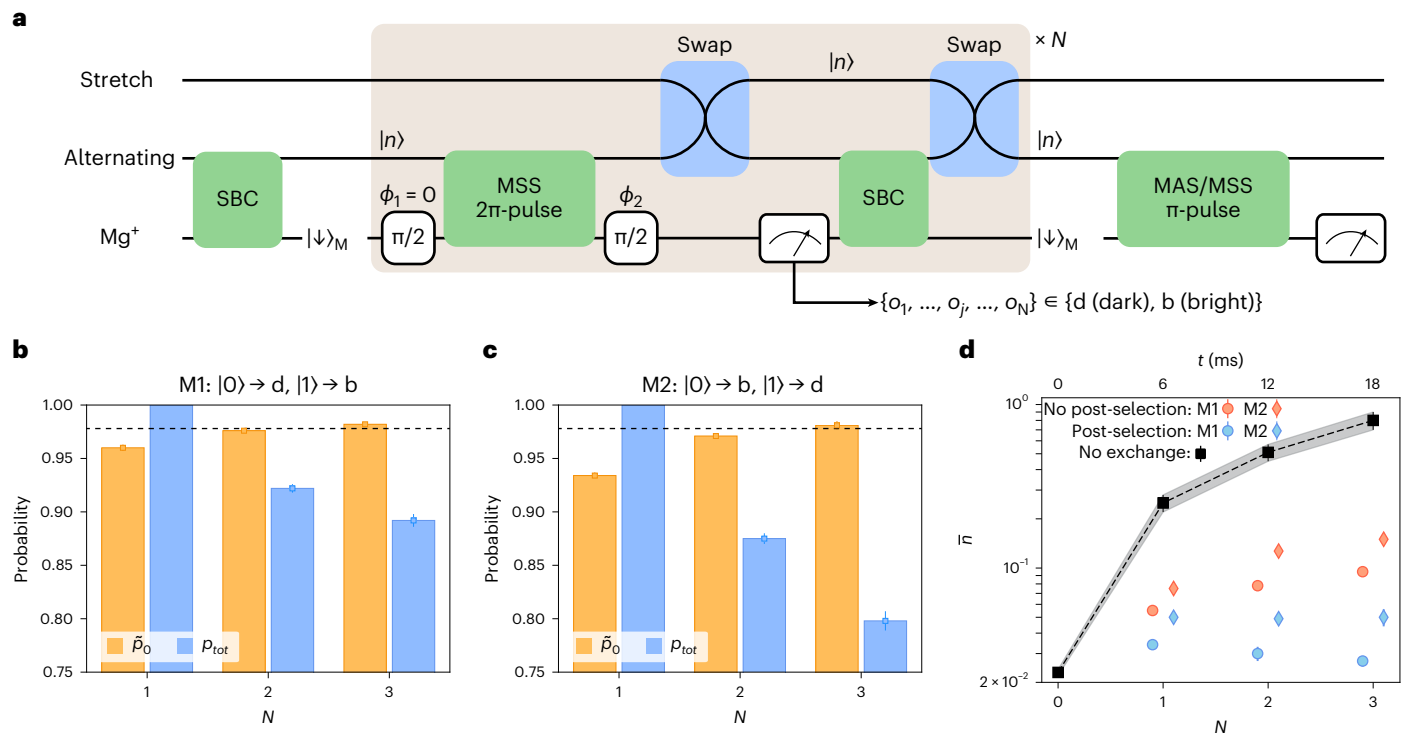
Fig. 3 | Repeated interrogation of a near-ground-state thermal distribution of trapped-ion motion. a, Pulse sequence for non-destructively distinguishing number states $\{|0\rangle, |1\rangle\}$. SBC, sideband cooling. See description in Main. **b,c**, Repeated measurement outcomes. With increasing N, the post-selected probability $\tilde{p}_0$ (orange bars) of determining the motional state to be $|0\rangle$ approaches the independently calibrated population p_0 (dashed line) in the initial motional state distribution. The similarity between mapping M1 (**b**), where few fluorescence photons are scattered when detecting $|0\rangle$, and mapping M2 (**c**), where thousands of fluorescence photons are scattered when detecting $|0\rangle$, shows the robustness of the protected state to photon recoil. The blue bars show p_{tot}, the total probability of post-selection (Main). **d**, Mean occupation number ($\bar{n}$) of the alternating mode (blue symbols) when post-selected on all N outcomes is lower than the corresponding $\bar{n}$ with no post-selection (red symbols). No-exchange $\bar{n}$ (black squares) was measured after applying a delay with the duration of N measurement blocks without swapping into the stretch mode. Each data point with a 68% confidence error bar was obtained from 6,000 experiments except for M2 $N = 3$, which was obtained from 2,000 experiments. Data points and bars are laterally offset from N values for legibility and error bars for some points are smaller than plot symbols.

other ion species. We can then perform a joint measurement of the mapped motional mode information for both modes in a single experimental trial, using a species-resolved state-dependent fluorescence read-out (Supplementary Section 4). The interaction given by equation (1) ideally conserves the total number $\mathcal{N}$ of phonons in both modes. Experimentally, only populations of states with the same $\mathcal{N}$ were found to be substantial, shown as dots in Fig. 2d–g along with simulation results (lines)[52] based on experimental parameters. The state preparation and measurement errors are larger in Fig. 2d–g compared to those in Fig. 2b,c because more complex pulse sequences were used during state preparation and read-out (Supplementary Section 4).

In Fig. 2d, with initial state $|1\rangle_A|0\rangle_S$ ($\mathcal{N} = 1$) the population swaps into $|0\rangle_A|1\rangle_S$, and we observe two anticorrelated sinusoidal population oscillations with similar amplitudes. At $t_{BS} \approx 50\,\mu s$, the coupling pulse realizes a beam-splitter operation $U_{BS} = \exp[i(\pi/4)(\hat{a}\hat{b}^\dagger + \hat{b}\hat{a}^\dagger)]$, which we expect to generate an entangled state $(|1\rangle_A|0\rangle_S + |0\rangle_A|1\rangle_S)/\sqrt{2}$. We observe approximately equal populations in $|0\rangle_A|1\rangle_S$ and $|1\rangle_A|0\rangle_S$ at t_{BS} and verify the coherence between these two components by performing a phonon interferometry experiment consisting of two beam-splitter operations with variable phase difference ϕ (Fig. 2e), which shows the coherence of the entangled state generated by the first beam-splitter pulse. We estimate an 84% confidence lower bound of the average fidelity in the one-phonon subspace of the beam-splitter operation to be 97.9% (Methods). The initial state $|1\rangle_A|1\rangle_S$ ($\mathcal{N} = 2$) evolves into $|0\rangle_A|2\rangle_S$ and $|2\rangle_A|0\rangle_S$ with nearly equal populations at t_{BS}, whereas the population in $|1\rangle_A|1\rangle_S$ is reduced almost to zero by destructive interference (Fig. 2f). This behaviour is analogous to Hong–Ou–Mandel

interference[22] but here phonons at different frequencies interfere. An entangled state of the form $(|2\rangle_A|0\rangle_S + |0\rangle_A|2\rangle_S)/\sqrt{2}$ is generated at t_{BS}, and the phase coherence of this state is also verified (Fig. 2g). Other conditional probabilities were tracked and are shown in Supplementary Figs. 4–7.

Atomic motion can be substantially perturbed by photon recoil during fluorescence-based internal state read-out. By limiting photon recoil to a certain ion j that does not participate in mode a, $\xi_{j,a}^{(i_a)} = 0$, this mode is protected and unperturbed by photon scattering from ion j. However, if ion j does not participate in mode a, mode a can also not be directly coupled with internal states of ion j. Mode coupling enables the state of mode a to be swapped into a suitable mode b, which can be coupled to the internal states of ion j, $\xi_{j,b}^{(i_b)} \neq 0$. Subsequently, information about the state of mode b can be coherently mapped to the internal states of ion j in such a way that the motional state is not altered. After swapping the motional state back into mode a, a read-out of ion j yields the encoded state information while preserving the state of mode a to a high degree aside from measurement projection.

As proof of principle, we implemented a protocol to non-destructively distinguish number states $|n\rangle \in \{|0\rangle, |1\rangle\}$ of ion motion using the circuit shown in Fig. 3a. When $|n\rangle$ is in the alternating mode, information can be mapped onto the Mg⁺ internal states with a Cirac–Zoller-type sequence[53] (schematically shown in the grey box; see Supplementary Section 7 for details) consisting of a motion-subtracting-sideband (MSS) 2π pulse surrounded by two carrier $\pi/2$ pulses. The MSS pulse ideally has no effect on $|0\rangle_A|\downarrow\rangle_M$ but transforms $|1\rangle_A|\downarrow\rangle_M$ into $-|1\rangle_A|\downarrow\rangle_M$. The two $\pi/2$ pulses turn this $|n\rangle_A$-dependent phase shift into

an $|n\rangle_A$-dependent population difference in the Mg$^+$ internal states $|\uparrow\rangle_M$ and $|\downarrow\rangle_M$. The state $|n\rangle_A$ is then swapped into $|n\rangle_S$ of the stretch mode, which does not couple to the Mg$^+$, followed by Mg$^+$ fluorescence detection, during which the state $|\downarrow\rangle_M$ scatters thousands of photons (outcome bright 'b'), whereas the state $|\uparrow\rangle_M$ scatters zero or very few photons (outcome dark 'd'). We can repeat the mapping and measurement sequence shown in the grey box by sideband cooling the in-phase and alternating modes near the ground state and swapping $|n\rangle_S$ back into the alternating mode. To test the resilience of the motional state to photon recoil during fluorescence detection, we performed repeated state measurements with two opposite state mappings M1 and M2, where M1 is $\{|0\rangle_A \to d, |1\rangle_A \to b\}$ and M2 is $\{|0\rangle_A \to b, |1\rangle_A \to d\}$.

In the experiments, the alternating mode was cooled to a thermal distribution with an average occupation $\bar{n} = 0.023(1)$, with probability $p_0 = 0.978(1)$ of being in $|0\rangle_A$, $p_1 = 0.022(1)$ in $|1\rangle_A$ and probability almost zero in higher number states. We repeated the motional state mapping and Mg$^+$ read-out up to three times and obtained a series of outcomes $\{o_1, \ldots, o_i, \ldots, o_N\}$ with $o_i \in \{d, b\}$, $i = 1, \ldots, N$. We post-selected only those trials where all N outcomes were the same (all d or all b) to improve state discrimination. The post-selected relative frequencies of declaring $|0\rangle$ and $|1\rangle$ are defined as $\tilde{p}_0 = p(\{d\}_N)/p_{tot}$ for M1 and $\tilde{p}_0 = p(\{b\}_N)/p_{tot}$ for M2, with $\tilde{p}_1 = 1 - \tilde{p}_0$. Here $p(\{d\}_N)$ and $p(\{b\}_N)$ are the probabilities of all N outcomes being d or b, respectively, and $p_{tot} = p(\{d\}_N) + p(\{b\}_N)$ is the total probability of post-selection.

The state after N rounds of interrogation can be characterized independently by applying a π pulse on the motion-adding-sideband (MAS) or MSS transition of the alternating mode, followed by another Mg$^+$ fluorescence detection. Assuming a thermal distribution of number states, the $\bar{n}$ can be estimated based on the sideband ratio averaged over a large number of outcomes[2].

The results for M1 are shown in Fig. 3b. With $N = 1$, $\tilde{p}_0 = p(\{d\}_N) = 0.960(3)$ (orange bar), which differs from the initial population p_0 by 0.02. We attribute this discrepancy to detection error, mainly due to spin decoherence during the mapping sequence. For $N = 2$ and $N = 3$, $\tilde{p}_0$ is very close to p_0 because the state was heralded several times, largely suppressing erroneous state declarations. However, we discarded an increasing fraction of trials (7.8% and 10.8%, respectively) in post-selection when outcomes from the several rounds disagreed. The discarded fraction was larger than that expected due to detection error alone, indicating that the motional state was changing slightly with increasing N, probably due to heating. The results with mapping M2 are displayed in Fig. 3c. Here $\tilde{p}_0 = p(\{b\}_N)$, and thousands of photons were scattered with each detection of $|0\rangle$. The relative frequencies $\tilde{p}_0$ also converged to the initial state population p_0, but more trials were discarded in post-selection, potentially due to imperfect protection of the stretch mode from Mg$^+$ scattering. We discarded 12.5% ($N = 2$) and 20.2% ($N = 3$) of all interrogations for M2. For larger N, heating during longer sequences increased leakage into higher number states, which lowered the read-out fidelity.

The $\bar{n}$ values of final motional states as determined by MAS/MSS transition probabilities are shown in Fig. 3d. The black data points show $\bar{n}$ when the motional state was left in the alternating mode for a duration equivalent to running N rounds of the measurement protocol. The increase in $\bar{n}$ was just due to heating of the mode. Red circles and red diamonds represent trials where the measurement blocks were executed with M1 and M2, respectively. The $\bar{n}$ values are reduced compared to just a delay (the black data points) because the motional state resided some of the time in the stretch mode, which has a lower heating rate. Blue circles and blue diamonds show $\bar{n}$ for trials post-selected on the measurement heralding $|0\rangle$ N times for M1 and M2. In all cases, M1 yielded the lowest $\bar{n}$, but post-selecting on M2, despite the large number of scattered photons, also yielded a reduced $\bar{n}$ compared to no post-selection. The difference between M1 and M2 may have arisen from residual recoil heating of the stretch mode, possibly from a non-zero z^3 contribution to the trapping potential (Supplementary

Section 6). Nevertheless, the stretch mode was still largely protected from recoil during the read-out and remained close to the state it was projected into during the interrogation. The complete datasets for all N and all measurement outcomes can be found in Supplementary Tables 1–6 and Supplementary Fig. 9.

Discussion and conclusion

Coherent coupling of normal modes of a mixed-species ion string can be used for cooling[49], indirect state preparation[54] and precision spectroscopy based on quantum logic[55]. Generating suitable spatial variation and strength for the couplings in larger ion crystals can be challenging for some mode pairs. This is generally improved by using smaller traps with more control electrodes. If direct coupling of two modes is challenging, one can couple several pairs of modes sequentially for operations such as state transfer. Our approach can be combined with spin-motion control techniques to enable new quantum simulations[56,57]. The non-destructive measurement protocol using protected modes can be adapted to measure any single bit of information about the motional state with an appropriate mapping sequence. This can be exploited for bosonic quantum-error-correction codes[9,11,16,42,58] and for other applications requiring repeated motional state measurement. Symmetric strings with $2N + 1$ ions have N protected modes that could be used in demonstrations of multimode entangled bosonic states.

Note that similar work on protected modes of trapped-ion crystals is underway in other research groups[59].

Online content

Any methods, additional references, Nature Portfolio reporting summaries, source data, extended data, supplementary information, acknowledgements, peer review information; details of author contributions and competing interests; and statements of data and code availability are available at https://doi.org/10.1038/s41567-024-02585-y.

References

1. Feynman, R. P. in *Feynman and Computation* (ed. Hey, A. J. G.) 133–153 (CRC Press, 2018).
2. Leibfried, D. et al. Trapped-ion quantum simulator: experimental application to nonlinear interferometers. *Phys. Rev. Lett.* **89**, 247901 (2002).
3. Porras, D. & Cirac, J. I. Bose–Einstein condensation and strong-correlation behavior of phonons in ion traps. *Phys. Rev. Lett.* **93**, 263602 (2004).
4. Bermudez, A., Schaetz, T. & Porras, D. Synthetic gauge fields for vibrational excitations of trapped ions. *Phys. Rev. Lett.* **107**, 150501 (2011).
5. Furusawa, A. et al. Unconditional quantum teleportation. *Science* **282**, 706–709 (1998).
6. Braunstein, S. L. Quantum error correction for communication with linear optics. *Nature* **394**, 47–49 (1998).
7. Ralph, T. C. Continuous variable quantum cryptography. *Phys. Rev. A* **61**, 010303 (1999).
8. van Loock, P. & Braunstein, S. L. Multipartite entanglement for continuous variables: a quantum teleportation network. *Phys. Rev. Lett.* **84**, 3482–3485 (2000).
9. Chuang, I. L., Leung, D. W. & Yamamoto, Y. Bosonic quantum codes for amplitude damping. *Phys. Rev. A* **56**, 1114–1125 (1997).
10. Knill, E., Laflamme, R. & Milburn, G. J. A scheme for efficient quantum computation with linear optics. *Nature* **409**, 46–52 (2001).
11. Gottesman, D., Kitaev, A. & Preskill, J. Encoding a qubit in an oscillator. *Phys. Rev. A* **64**, 012310 (2001).
12. Braunstein, S. L. & van Loock, P. Quantum information with continuous variables. *Rev. Mod. Phys.* **77**, 513–577 (2005).
13. Kok, P. et al. Linear optical quantum computing with photonic qubits. *Rev. Mod. Phys.* **79**, 135–174 (2007).

14. Lloyd, S. & Braunstein, S. L. Quantum computation over continuous variables. *Phys. Rev. Lett.* **82**, 1784–1787 (1999).
15. Braunstein, S. L. Error correction for continuous quantum variables. *Phys. Rev. Lett.* **80**, 4084–4087 (1998).
16. Michael, M. H. et al. New class of quantum error-correcting codes for a bosonic mode. *Phys. Rev. X* **6**, 031006 (2016).
17. Brown, K. R. et al. Coupled quantized mechanical oscillators. *Nature* **471**, 196–199 (2011).
18. Harlander, M., Lechner, R., Brownnutt, M., Blatt, R. & Hänsel, W. Trapped-ion antennae for the transmission of quantum information. *Nature* **471**, 200–203 (2011).
19. Wilson, A. C. et al. Tunable spin–spin interactions and entanglement of ions in separate potential wells. *Nature* **512**, 57–60 (2014).
20. Toyoda, K., Hiji, R., Noguchi, A. & Urabe, S. Hong–Ou–Mandel interference of two phonons in trapped ions. *Nature* **527**, 74–77 (2015).
21. Gorman, D. J., Schindler, P., Selvarajan, S., Daniilidis, N. & Häffner, H. Two-mode coupling in a single-ion oscillator via parametric resonance. *Phys. Rev. A* **89**, 062332 (2014).
22. Hong, C. K., Ou, Z. Y. & Mandel, L. Measurement of subpico-second time intervals between two photons by interference. *Phys. Rev. Lett.* **59**, 2044–2046 (1987).
23. Rauschenbeutel, A. et al. Controlled entanglement of two field modes in a cavity quantum electrodynamics experiment. *Phys. Rev. A* **64**, 050301 (2001).
24. Gröblacher, S., Hammerer, K., Vanner, M. R. & Aspelmeyer, M. Observation of strong coupling between a micromechanical resonator and an optical cavity field. *Nature* **460**, 724–727 (2009).
25. Teufel, J. D. et al. Circuit cavity electromechanics in the strong-coupling regime. *Nature* **471**, 204–208 (2011).
26. Wang, H. et al. Deterministic entanglement of photons in two superconducting microwave resonators. *Phys. Rev. Lett.* **106**, 060401 (2011).
27. Zakka-Bajjani, E. et al. Quantum superposition of a single microwave photon in two different 'colour' states. *Nat. Phys.* **7**, 599–603 (2011).
28. Verhagen, E., Deléglise, S., Weis, S., Schliesser, A. & Kippenberg, T. J. Quantum-coherent coupling of a mechanical oscillator to an optical cavity mode. *Nature* **482**, 63–67 (2012).
29. Shalabney, A. et al. Coherent coupling of molecular resonators with a microcavity mode. *Nat. Commun.* **6**, 5981 (2015).
30. Gao, Y. Y. et al. Programmable interference between two microwave quantum memories. *Phys. Rev. X* **8**, 021073 (2018).
31. Capmany, J. & Pérez, D. *Programmable Integrated Photonics* (Oxford Univ. Press, 2020).
32. Palomaki, T., Harlow, J., Teufel, J., Simmonds, R. & Lehnert, K. W. Coherent state transfer between itinerant microwave fields and a mechanical oscillator. *Nature* **495**, 210–214 (2013).
33. Kotler, S. et al. Direct observation of deterministic macroscopic entanglement. *Science* **372**, 622–625 (2021).
34. Chapman, B. J. et al. High-on-off ratio beam-splitter interaction for gates on bosonically encoded qubits. *PRX Quantum* **4**, 020355 (2023).
35. Lu, Y. et al. High-fidelity parametric beamsplitting with a parity-protected converter. *Nat. Commun.* **14**, 5767 (2023).
36. Wineland, D. J. et al. Experimental issues in coherent quantum-state manipulation of trapped atomic ions. *J. Res. Natl Inst. Stand. Technol.* **103**, 259–328 (1998).
37. Leibfried, D., Blatt, R., Monroe, C. & Wineland, D. Quantum dynamics of single trapped ions. *Rev. Mod. Phys.* **75**, 281–324 (2003).
38. Heeres, R. W. et al. Implementing a universal gate set on a logical qubit encoded in an oscillator. *Nat. Commun.* **8**, 94 (2017).
39. Gao, Y. Y. et al. Entanglement of bosonic modes through an engineered exchange interaction. *Nature* **566**, 509–512 (2019).
40. Sivak, V. et al. Real-time quantum error correction beyond break-even. *Nature* **616**, 50–55 (2023).
41. Ni, Z. et al. Beating the break-even point with a discrete-variable-encoded logical qubit. *Nature* **616**, 56–60 (2023).
42. Flühmann, C. et al. Encoding a qubit in a trapped-ion mechanical oscillator. *Nature* **566**, 513–517 (2019).
43. de Neeve, B., Nguyen, T.-L., Behrle, T. & Home, J. P. Error correction of a logical grid state qubit by dissipative pumping. *Nat. Phys.* **18**, 296–300 (2022).
44. Kienzler, D. et al. Observation of quantum interference between separated mechanical oscillator wave packets. *Phys. Rev. Lett.* **116**, 140402 (2016).
45. Gan, H., Maslennikov, G., Tseng, K.-W., Nguyen, C. & Matsukevich, D. Hybrid quantum computing with conditional beam splitter gate in trapped ion system. *Phys. Rev. Lett.* **124**, 170502 (2020).
46. Jost, J. D. et al. Entangled mechanical oscillators. *Nature* **459**, 683–685 (2009).
47. Wolf, F. et al. Non-destructive state detection for quantum logic spectroscopy of molecular ions. *Nature* **530**, 457–460 (2016).
48. Wineland, D. & Dehmelt, H. Principles of the stored ion calorimeter. *J. Appl. Phys.* **46**, 919–930 (1975).
49. Hou, P.-Y. et al. Indirect cooling of weakly coupled trapped-ion mechanical oscillators. *Phys. Rev. X* **14**, 021003 (2023).
50. James, D. F. V. Quantum dynamics of cold trapped ions with application to quantum computation. *Appl. Phys. B* **2**, 181–190 (1998).
51. Blakestad, R. B. *Transport of Trapped-ion Qubits Within a Scalable Quantum Processor*. PhD thesis, California Institute of Technology (2002).
52. Johansson, J. R., Nation, P. D. & Nori, F. QuTiP 2: a Python framework for the dynamics of open quantum systems. *Comput. Phys. Commun.* **184**, 1234–1240 (2013).
53. Cirac, J. I. & Zoller, P. Quantum computations with cold trapped ions. *Phys. Rev. Lett.* **74**, 4091–4094 (1995).
54. Chou, C.-W. et al. Preparation and coherent manipulation of pure quantum states of a single molecular ion. *Nature* **545**, 203–207 (2017).
55. Schmidt, P. O. et al. Spectroscopy using quantum logic. *Science* **309**, 749–752 (2005).
56. Hartmann, M. J., Brandao, F. G. & Plenio, M. B. Strongly interacting polaritons in coupled arrays of cavities. *Nat. Phys.* **2**, 849–855 (2006).
57. Greentree, A. D., Tahan, C., Cole, J. H. & Hollenberg, L. C. Quantum phase transitions of light. *Nat. Phys.* **2**, 856–861 (2006).
58. Leghtas, Z. et al. Hardware-efficient autonomous quantum memory protection. *Phys. Rev. Lett.* **111**, 120501 (2013).
59. Metzner, J. et al. Using 'protected' modes in trapped ions to enable mid-algorithm measurements for CVQC. *Bull. Am. Phys. Soc.* **66**, C10.00006 (2021).

Methods

Derivation of the coupling Hamiltonian

We consider a linear string consisting of N ions, with possibly different masses M_n and charges Q_n for $n \in \{1, ..., N\}$, trapped in a three-dimensional potential well $U_0(\mathbf{r})$ formed by externally applied potentials. We choose a coordinate system (x, y, z) that is aligned with the principal axes of the equipotential ellipsoid that characterizes $U_0(\mathbf{r})$ near its minimum position, which we define as the origin of the coordinate system. As shown in Fig. 1b, x and y point from the ion positions towards the control and radio-frequency electrodes, and z is along the trap axis, which runs parallel to the electrode edges. The coordinate origin is in the plane parallel to and midway between the electrode wafers and coincides with the minimum of the harmonic potential (black line) sketched in Fig. 1c. The coordinate axes line up with the eigenvectors of three groups of normal (decoupled) motional modes, with N modes in each group, which we will derive next. The total potential energy for N ions in the potential well at positions $\mathbf{r}_n = (r_{x,n}, r_{y,n}, r_{z,n})^\mathsf{T}$ is given by

$$U_{\text{pot}}(\mathbf{r}_1, ... \mathbf{r}_N) = \sum_{n=1}^{N} Q_n U_0(\mathbf{r}_n) + \sum_{n=1}^{N} \sum_{n'>n}^{N} \frac{Q_n Q_{n'}}{4\pi\epsilon_0 |\mathbf{r}_n - \mathbf{r}_{n'}|}. \quad (5)$$

By simultaneously solving $\partial U_{\text{pot}}/\partial \mathbf{r}_n = 0$ for all n, we obtain each ion's equilibrium position $\mathbf{r}_n^{(0)}$. We then expand U_{pot} to second order in small mass-weighted coordinates changes $q_{i,n} = (r_{i,n} - r_{i,n}^{(0)})/\sqrt{M_n}$ with $i \in \{x, y, z\}$ around $\mathbf{r}_n^{(0)}$. On diagonalizing the resulting Hessian matrix, we obtain $3N$ mutually decoupled normal modes of ion motion with frequencies $\omega_{i,k}$ and quantized normal mode coordinates:

$$u_{i,k} = \sqrt{\frac{\hbar}{2\omega_{i,k}}} \left(\hat{a}_{i,k} + \hat{a}_{i,k}^\dagger\right),$$

where $\omega_{i,k}$, $\hat{a}_{i,k}^\dagger$ and $\hat{a}_{i,k}$ are the motional frequency, creation operator and annihilation operator, respectively, of the kth mode along axis $i \in \{x, y, z\}$. In the normal mode coordinates, the Hamiltonian of the motion of an ion string consists of $3N$ uncoupled HOs and can be written as

$$H_0 = \sum_{i \in \{x,y,z\}} \sum_{k=1}^{N} \hbar\omega_{i,k} \left(\hat{a}_{i,k}^\dagger \hat{a}_{i,k} + 1/2\right).$$

Each ion oscillates around its equilibrium position but does not participate in all normal modes equally in general and may not participate at all in some modes. For the nth ion, the displacement along the ith axis $\hat{q}_{i,n}$ can be written in terms of the kth normal mode creation and annihilation operators as

$$\hat{q}_{i,n} = \sum_{k=1}^{N} \sqrt{\frac{\hbar}{2M_n\omega_{i,k}}} \xi_{n,k}^{(i)} \left(\hat{a}_{i,k} + \hat{a}_{i,k}^\dagger\right), \quad (6)$$

where $\xi_{n,k}^{(i)}$ is the transformation matrix element between the spatial coordinates of the nth ion displacement $q_{i,n}$ along axis i and the normal mode vector component along the same axis for the kth eigenmode.

To couple two particular normal modes—mode a oscillating at frequency $\omega_{i_a,a}$ along axis i_a and mode b at frequency $\omega_{i_b,b}$ along axis i_b—we can apply an oscillating perturbing potential $U_{\text{mod}}(\mathbf{r}, t) = U_{\text{m}}(\mathbf{r}) \cos(\omega t + \phi)$ with ω close to the frequency difference of the modes we would like to couple, $\omega \approx \omega_{i_a,a} - \omega_{i_b,b}$. Expanding $U_{\text{m}}(\mathbf{r})$ up to second order around a certain position $\mathbf{r}_0$, we obtain

$$U_{\text{m}}(\mathbf{r}_0 + \delta\mathbf{r}) \approx U_{\text{m}}(\mathbf{r}_0) + \sum_{i \in \{x,y,z\}} \frac{\partial U_{\text{m}}}{\partial i}\bigg|_{\mathbf{r}=\mathbf{r}_0} \delta r_i + \frac{1}{2} \sum_{i,j \in \{x,y,z\}} \frac{\partial^2 U_{\text{m}}}{\partial i \, \partial j}\bigg|_{\mathbf{r}=\mathbf{r}_0} \delta r_i \, \delta r_j. \quad (7)$$

Anticipating that only terms proportional to $\delta r_{i_a} \delta r_{i_b}$ of the two normal modes we desire to couple will rotate slowly in the interaction picture with respect to H_0, we can drop all other terms in the expansion of $U_{\text{m}}(\mathbf{r})$:

$$U_{\text{m}}(\mathbf{r}_0 + \delta\mathbf{r}) \approx 2^{-\delta(i_a, i_b)} \frac{\partial^2 U_{\text{m}}}{\partial i_a \partial i_b}\bigg|_{\mathbf{r}=\mathbf{r}_0} \delta r_{i_a} \, \delta r_{i_b}.$$

Here, $\delta(i_a, i_b) = 1$ for $i_a = i_b$ and 0 otherwise, and we have used $\partial^2 U_{\text{m}}/(\partial i_a \partial i_b) = \partial^2 U_{\text{m}}/(\partial i_b \partial i_a)$. In practice, the dropped terms may cause an undesirable distortion of the potential and excess ion motion and should be minimized when designing the perturbing potential. Again keeping only near-resonant terms, inserting the displacement operators for displacements of the nth ion in modes a and b, namely $\delta r_{i_a,n} = \hat{q}_{i_a,n}$ and $\delta r_{i_b,n} = \hat{q}_{i_b,n}$, abbreviating $\partial^2 U_{\text{m}}/(\partial i_a \partial i_b)|_{\mathbf{r}=\mathbf{r}_n^{(0)}} \equiv \alpha_n$ and inserting equation (6), the Hamiltonian from the perturbing potential can be approximated as

$$\begin{aligned}
H &= \sum_{n=1}^{N} Q_n U_{\text{mod}}(\mathbf{r}_n, t) \\
&\approx \sum_{n=1}^{N} Q_n 2^{-\delta(i_a, i_b)} \alpha_n \hat{q}_{i_a,n} \hat{q}_{i_b,n} \cos(\omega t + \phi) \\
&= \sum_{n=1}^{N} Q_n 2^{-\delta(i_a, i_b)} \alpha_n \left[\sum_{k=1}^{N} \sqrt{\frac{\hbar}{2M_n\omega_{i_a,k}}} \xi_{n,k}^{(i_a)} \left(\hat{a}_{i_a,k} + \hat{a}_{i_a,k}^\dagger\right)\right] \\
&\quad \times \left[\sum_{l=1}^{N} \sqrt{\frac{\hbar}{2M_n\omega_{i_b,l}}} \xi_{n,l}^{(i_b)} \left(\hat{a}_{i_b,l} + \hat{a}_{i_b,l}^\dagger\right)\right] \\
&\quad \times \frac{1}{2}\left(e^{-i(\omega t + \phi)} + e^{i(\omega t + \phi)}\right) \\
&= \sum_{n,k,l=1}^{N} 2^{-\delta(i_a, i_b)} \frac{\hbar Q_n \alpha_n}{4M_n\sqrt{\omega_{i_a,k}\omega_{i_b,l}}} \xi_{n,k}^{(i_a)} \xi_{n,l}^{(i_b)} \left(\hat{a}_{i_a,k} + \hat{a}_{i_a,k}^\dagger\right)\left(\hat{a}_{i_b,l} + \hat{a}_{i_b,l}^\dagger\right) \\
&\quad \times \left(e^{-i(\omega t + \phi)} + e^{i(\omega t + \phi)}\right).
\end{aligned} \quad (8)$$

We analyse this expression in the interaction frame with respect to H_0 by replacing $\hat{a}_{i,k} \rightarrow \hat{a}_{i,k} \, e^{-i\omega_{i,k}t}$ and $\hat{a}_{i,k}^\dagger \rightarrow \hat{a}_{i,k}^\dagger \, e^{i\omega_{i,k}t}$. When $\omega = \omega_{i_a,a} - \omega_{i_b,b}$, we can neglect all terms that are not rotating at $\pm[\omega - (\omega_{i_a,a} - \omega_{i_b,b})]$, which simplifies the coupling Hamiltonian in equation (8) to

$$H = \hbar g_0 \left(e^{i\phi} \, \hat{a}\hat{b}^\dagger + e^{-i\phi} \, \hat{a}^\dagger\hat{b}\right), \quad (9)$$

where we use $\omega_{i_a,a} = \omega_a$, $\omega_{i_b,b} = \omega_b$, $\hat{a}_{i_a,a} = \hat{a}$ and $\hat{a}_{i_b,b} = \hat{b}$ for simplicity from this point onward. Note that coupling two modes along the same axis, $i_a = i_b$, results in two near-resonant cross-terms proportional to $\xi_{n,a}^{(i_a)} \xi_{n,b}^{(i_a)}$ and $\xi_{n,b}^{(i_a)} \xi_{n,a}^{(i_a)}$ that both contribute to the coupling equally and cancel the factor $2^{-\delta(i_a, i_a)}$. The coupling strength is

$$g_0 = \sum_{n=1}^{N} g_n = \sum_{n=1}^{N} \frac{Q_n \alpha_n}{4M_n\sqrt{\omega_a\omega_b}} \xi_{n,a}^{(i_a)} \xi_{n,b}^{(i_b)}. \quad (10)$$

This is identical to equation (4).

Time evolution of coupled motional states

When two modes represented by ladder operators $\hat{a}$ and $\hat{b}$ are coupled by the Hamiltonian in equation (9), their states of motion will become entangled and, after an exchange of population, disentangled, in a periodic fashion. The time-dependent states can be found by first performing a basis transformation:

$$\hat{c}_+ = \frac{1}{\sqrt{2}}\left(\hat{a} + e^{-i\phi}\,\hat{b}\right),$$

$$\hat{c}_- = \frac{1}{\sqrt{2}}\left(\hat{a} - e^{-i\phi}\,\hat{b}\right), \quad (11)$$

which diagonalizes the interaction Hamiltonian:

$$\hbar g_0 \left(e^{i\phi} \, \hat{a}\hat{b}^\dagger + e^{-i\phi} \, \hat{a}^\dagger \hat{b} \right) = \hbar g_0 \left(\hat{c}_+^\dagger \hat{c}_+ - \hat{c}_-^\dagger \hat{c}_- \right). \tag{12}$$

The right-hand side represents two HOs with energies separated by twice the interaction energy $\hbar g_0$. In the interaction frame of reference, these oscillators have simple equations of motion:

$$\hat{c}_\pm^\dagger(t) = \hat{c}_\pm^\dagger(0) \exp(\pm i g_0 t). \tag{13}$$

Writing $\hat{a}^\dagger(0) = \hat{a}^\dagger$ and $\hat{b}^\dagger(0) = \hat{b}^\dagger$ for brevity and inserting the time dependence into the equations for $\hat{a}(t)$ and $\hat{b}(t)$ yields

$$\hat{a}^\dagger(t) = \hat{a}^\dagger \cos(g_0 t) + i \, e^{i\phi} \, \hat{b}^\dagger \sin(g_0 t),$$
$$\hat{b}^\dagger(t) = \hat{b}^\dagger \cos(g_0 t) + i \, e^{-i\phi} \, \hat{a}^\dagger \sin(g_0 t). \tag{14}$$

Any state of the oscillators at time t can be written as a superposition of number states with complex amplitudes c_{mn} by acting with different combinations of creation operators on the vacuum state $|0\rangle_a |0\rangle_b$,

$$|\Psi_a(t)\rangle |\Phi_b(t)\rangle = \sum_{m,n=0}^{\infty} \frac{c_{mn}}{\sqrt{m!n!}} \left[\hat{a}^\dagger(t)\right]^m \left[\hat{b}^\dagger(t)\right]^n |0\rangle_a |0\rangle_b, \tag{15}$$

such that the time dependence is fully captured in the creation operators. For general times t, this implies a rather complicated entangled state of the modes, which becomes simpler for certain evolution times. For example, when setting $\tau_{BS} = \pi/(4g_0)$, the trigonometric factors $\sin(g_0 \tau_{BS}) = \cos(g_0 \tau_{BS}) = 1/\sqrt{2}$ and equation (14) turns into a beam-splitter relation[60] that can be used to demonstrate the Hong–Ou–Mandel effect, here for two modes at different frequencies in a mixed-species string of ions (Main and Fig. 2f,g).

Equation (14) simplifies even more for $\tau_k = k\pi/(2g_0)$ with k a positive integer. For k odd this yields:

$$\hat{a}^\dagger(\tau_k) = i \, e^{i(g_0 \tau_k + \phi)} \, \hat{b}^\dagger,$$
$$\hat{b}^\dagger(\tau_k) = i \, e^{i(g_0 \tau_k - \phi)} \, \hat{a}^\dagger, \tag{16}$$

which implies that $|\Psi_a(\tau_k)\rangle |\Phi_b(\tau_k)\rangle$ with k odd has the original states of modes a and b swapped and shifted by a phase $g_0 \tau_k$ per phonon, plus or minus ϕ. This phase difference arises relative to that of the uncoupled evolution of the modes and can be thought of as a consequence of the coupling that modifies the energies of the eigenstates with the other factors due to the phase ϕ of the applied drive. For k even:

$$\hat{a}^\dagger(\tau_k) = e^{i g_0 \tau_k} \, \hat{a}^\dagger,$$
$$\hat{b}^\dagger(\tau_k) = e^{i g_0 \tau_k} \, \hat{b}^\dagger, \tag{17}$$

which signifies one or several complete forth-and-back exchanges and a phase shift due to the coupling energy. Up to this phase shift, the state $|\Psi_a(\tau_k)\rangle |\Phi_b(\tau_k)\rangle$ with k even is identical to the one at $t = 0$ in the interaction frame of reference.

Coupling drive generation and control

We used a segmented linear Paul trap consisting of a pair of radio-frequency electrodes and 47 control electrodes[51]. The voltages of the control electrodes were produced by 47 independent arbitrary waveform generators (AWGs) with 16 bit resolution running at 50 megasamples per second[61]. Each AWG output was connected to a control electrode through a two-stage low-pass filter with a 3 dB corner frequency of about 50 kHz to suppress noise at motional frequencies. The oscillating potential $U(\mathbf{r}, t)$ for creating

mode–mode coupling was produced by applying suitable voltages to the 12 electrodes nearest to the ions using the corresponding AWG channels. The oscillating signals were added to the static voltages that produced the axial confinement. The AWGs were not actively synchronized but had approximately equal clock speeds, so we reset their phase at the beginning of each experiment to ensure all the drives oscillated in phase. The coupling of motional modes became ineffective for motional frequency differences larger than 1 MHz due to attenuation from the low-pass filters and the 1 MHz bandwidth of the AWG output amplifiers.

We shaped the amplitude envelope of the coupling pulses to suppress the off-resonant excitation of other normal modes due to the spectral side-lobes of the modulation pulses. The pulse amplitude ramped up as approximately $\sin^2(2\pi f t)$, with $f = 12.5$ kHz and $0 \leq t \leq 20$ μs, at the beginning of the pulse and ramped back to zero using a time-reversed copy of the ramp-up. We observed substantial off-resonant excitation of the axial in-phase mode (at ~1.5 MHz) of a $^9\mathrm{Be}^+$–$^{25}\mathrm{Mg}^+$–$^9\mathrm{Be}^+$ crystal when using a square-shaped coupling pulse near the resonant frequency of the alternating–stretch coupling, while such excitation was largely suppressed with shaped pulses.

We determined the coupling drive amplitudes for the 12 electrodes using a trap potential simulation[51]. The potential of each electrode was modelled using the boundary element method[62]. We calculated the total potential around the centre of an ion crystal by summing the potential from all 12 electrodes. We optimized the voltages to generate a potential for which the desired spatial derivative was maximized while the unwanted components were minimized. These unwanted terms typically included the gradients $\partial U_m/\partial i$, $i \in \{x, y, z\}$, which displace and potentially heat the ion motion, and the curvatures $\partial^2 U_m/\partial i^2$, $i \in \{x, y, z\}$, which modulate motional frequencies. The undesired curvatures could not be eliminated due to the constraint from the Laplace equation $\nabla^2 U_m = 0$, but they could be chosen to be far off-resonant. Higher-order derivatives of the potential were typically negligible in our trap and were not considered in the simulations.

Data availability
Source data are provided with this paper. All other data that support the plots within this paper are available from the corresponding authors upon reasonable request.

Code availability
The simulation and analysis codes are available from the corresponding authors upon reasonable request.

References
60. Caves, C. M. Quantum-mechanical noise in an interferometer. *Phys. Rev. D* **23**, 1693 (1981).
61. Bowler, R., Warring, U., Britton, J. W., Sawyer, B. & Amini, J. Arbitrary waveform generator for quantum information processing with trapped ions. *Rev. Sci. Instrum.* **84**, 033108 (2013).
62. Sadiku, M. N. *Numerical Techniques in Electromagnetics* (CRC Press, 2000).

Author contributions

Competing interests

The authors declare no competing interests.

Additional information